2D MATERIALS

Visualizing broken symmetry and topological defects in a quantum Hall ferromagnet

Xiaomeng Liu[1]†, Gelareh Farahi[1]†, Cheng-Li Chiu[1]†, Zlatko Papic[2], Kenji Watanabe[3], Takashi Taniguchi[4], Michael P. Zaletel[5], Ali Yazdani[1]*

The interaction between electrons in graphene under high magnetic fields drives the formation of a rich set of quantum Hall ferromagnetic (QHFM) phases with broken spin or valley symmetry. Visualizing atomic-scale electronic wave functions with scanning tunneling spectroscopy (STS), we resolved microscopic signatures of valley ordering in QHFM phases and spectral features of fractional quantum Hall phases of graphene. At charge neutrality, we observed a field-tuned continuous quantum phase transition from a valley-polarized state to an intervalley coherent state, with a Kekulé distortion of its electronic density. Mapping the valley texture extracted from STS measurements of the Kekulé phase, we could visualize valley skyrmion excitations localized near charged defects. Our techniques can be applied to examine valley-ordered phases and their topological excitations in a wide range of materials.

Quantum Hall ferromagnets are broken-symmetry states in which the exchange interaction between electrons in Landau levels gives rise to quantum Hall phases with polarized or coherent superposition of spin, valley, or orbital degrees of freedom (*1*). In the presence of a magnetic field, a variety of two-dimensional electronic systems—including those in semiconductors (*1*, *2*), graphene (*2*), and an increasing number of moiré flat-band materials—host a diversity of quantum Hall ferromagnetic (QHFM) phases (*3*–*8*). Thus far, these interacting and topological phases of matter have been examined macroscopically, usually through study of their transport properties. However, the microscopic features of the electronic wave functions of these phases can directly reveal the nature of their broken symmetry (*9*, *10*) and, more important, can determine the nature of the excitations they host. A particularly interesting aspect of broken-symmetry states is their topological excitations, such as skyrmions (*11*–*13*), which determine the stability of such phases, and whose interactions may lead to the formation of more exotic quantum phases, such as the skyrmion superconductivity recently proposed in moiré materials (*14*–*16*).

Monolayer graphene's SU(4) isospin space, consisting of spin and valley, gives rise to a rich array of QHFM phases, which have been studied using transport and thermodynamic measurements (*2*). Particularly intriguing is the electrically insulating phase at the charge neutrality point at high magnetic fields (*17*), because with two of four isospin flavors occupied, Pauli exclusion prevents spin and valley from being simultaneously polarized. Theoretical efforts have predicted a rich phase diagram of four possible broken-symmetry QHFM states at charge neutrality (*18*): a charge density wave (CDW) phase, which is sublattice- and valley-polarized and spin-unpolarized; the spin ferromagnet (FM), which is a quantum spin Hall insulator; the canted antiferromagnet (CAF), in which spins on different sublattices point in near-opposite directions; and an intervalley coherent (IVC) state with a Kekulé reconstruction, which is spin-unpolarized. A recent theory also proposed the coexistence of CAF and IVC (*19*). Although transport studies have constrained aspects of the phase diagram (*20*, *21*), the nature of the ground state of graphene at charge neutrality has remained unresolved in the absence of microscopic measurements that probe the order parameter. Also unexplored are the plethora of topological excitations that these phases have been predicted to host, such as a variety of skyrmions, which may have complex flavor textures and may even harbor fractional charge on the scale of the magnetic length (*22*–*25*). Here, we used spectroscopic mapping to visualize the broken-symmetry states in graphene as a function of carrier concentration, including at charge neutrality, where we find evidence for localized valley skyrmions within the Kekulé phase. Our work demonstrates the power of spectroscopic imaging to detect valley ordering and topological excitations of valley orders; the method is applicable to a wide range of two-dimensional materials and their heterostructures.

The monolayer graphene devices used for our studies are fabricated on hexagonal boron nitride (hBN) substrates, with either graphite (devices A and C) or silicon back gates (device B) (see Fig. 1 for the experimental setup and an optical image of device A). All samples show similar spectroscopic properties, except that the fractional quantum Hall features are visible only in the graphite gate samples (devices A and C) (*26*). Figure 1, B and C, shows measurements of differential conductance dI/dV as function of sample bias V_B measured over a wide range of filling factors ν ($\nu = 2\pi n l_B^2$, where $l_B = \sqrt{\hbar/eB}$ is the magnetic length, n is the carrier density, $\hbar$ is the reduced Planck's constant, e is elementary charge, and B is the magnetic field); the filling factor is controlled by the back gate voltage V_g. The Landau levels (LLs) can be identified by their peaks in dI/dV; the energy corresponds to $E_N = \hbar\omega_c\sqrt{N}$, where N is the LL orbital index and $\hbar\omega_c \sim 110$ mV is the extracted cyclotron energy from fitting Fig. 1D. This cyclotron gap corresponds to that calculated with a renormalized Fermi velocity of 1.26×10^6 m/s, similar to the values found in previous studies (*27*). As the filling factor increases, the Fermi energy is pinned within a LL as it is being filled and then jumps to the next LL at $\nu = \pm 2, \pm 6, \pm 10$. For the incompressible states formed at these fillings, we find that energy gaps across the Fermi energy are enlarged by a factor of ~2 relative to the expected cyclotron gap (fig. S1). This effect, which does not depend on setpoint conditions, is likely caused by the graphene's bulk insulating behavior when the chemical potential lies within these gaps [see discussion in (*26*)].

Symmetry-breaking states driven by electron-electron interaction are clearly demonstrated in our spectroscopic measurements by gaps at all the intermediate integer fillings (Fig. 1C). The sizes of the gaps in our experiment at symmetry-breaking states and single-particle quantum Hall states were larger than those observed in transport and thermodynamic studies. We find that tip-induced band bending is negligible in most of our measurements, which likely contributes to our ability to observe symmetry-breaking gaps. Although we occasionally find tips that show a signature of band bending in spectroscopic measurements (*26*) similar to previous studies (*27*–*38*), datasets we obtained with improved tip conditions demonstrate the following differences: (i) Our data (Fig. 1C) does not show any Coulomb diamond features associated with a tip-induced quantum dot, as seen in previous studies (*34*). (ii) Our sample is not doped by impurities and our measurements are not influenced by a tip-sample work function mismatch, as shown by the observation that charge neutrality occurs near zero gate voltage. (iii) V_B does not influence carrier density in the probed area; the dashed lines in Fig. 1C marking incompressible states are nearly vertical, therefore showing that tip gating is negligible. (iv) At partial fillings, the LLs are always pinned to the Fermi energy with their jumps aligned with the occurrence of the

[1]Joseph Henry Laboratories and Department of Physics, Princeton University, Princeton, NJ 08544, USA. [2]School of Physics and Astronomy, University of Leeds, Leeds LS2 9JT, UK. [3]Research Center for Functional Materials, National Institute for Materials Science, 1-1 Namiki, Tsukuba 305-0044, Japan. [4]International Center for Materials Nanoarchitectonics, National Institute for Materials Science, 1-1 Namiki, Tsukuba 305-0044, Japan. [5]Department of Physics, University of California, Berkeley, CA 94720, USA.
*Corresponding author. Email: yazdani@princeton.edu
†These authors contributed equally to this work.

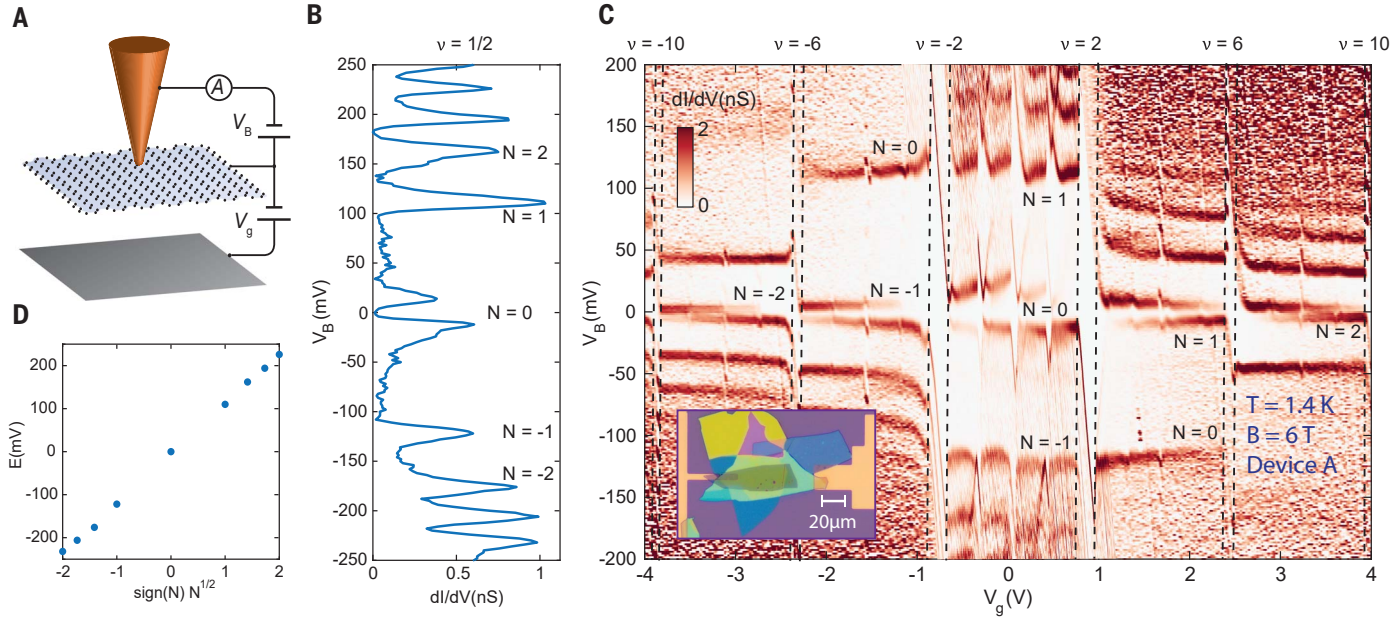

Fig. 1. Experimental setup and large gate range spectra. (**A**) Schematic of the STM measurement setup. The orange cone represents the tip, the light blue plane denotes the graphene, and the gray plane denotes the bottom gate. The bottom gate voltage V_g tunes the carrier density of graphene; V_B changes the bias voltage between the tip and graphene. (**B**) Spectrum of device A at ν = 1/2 showing LL peaks of different orbital numbers *N*. (**C**) Tunneling spectra of device A as a function of bias voltage and gate voltage measured at B = 6 T, T = 1.4 K at a fixed tip height. Inset: Optical image of device A. The left gold pad contacts the graphite gate; the right contact connects with graphene. (**D**) The energy of LLs extracted from the data in (B), displaying good agreement with $E_N = \hbar\omega_c\sqrt{N}$.

incompressible states, which suggests that there is no density mismatch between the probed area and the bulk of the sample. It is possible that our tip effective radius is small relative to the magnetic length, so that the work function mismatch between the tip and sample (which would typically lead to band bending) traps at most one electron charge below the tip, rather than producing a well-defined change in filling factor in a larger region.

Beyond resolving the presence of broken-symmetry states, our experiments also show a direct signature of fractional quantum Hall (FQH) phases in spectroscopic measurements. Focusing on the scanning tunneling spectroscopy (STS) properties between ν = −2 and 2, as shown in Fig. 2A, we resolve enlarged gaps at partial filling of the zeroth LL (ZLL) corresponding to the fractional quantum Hall states at ν = ±2/3, ±1/3. We corroborate the formation of FQH states in our devices by performing transport measurement while the tip height is reduced from the tunneling condition to directly contact the monolayer graphene (Fig. 2B). In this Corbino geometry, measurements of the conductance of our sample show dips at fractional fillings associated with the formation of FQH states. The observation of rich fractional states including ν = 4/9 in our samples, at a modest magnetic field (6 T) and at relatively elevated temperature (1.4 K), attests to their high quality, making them comparable to the fully hBN-encapsulated and dual graphite–gated devices used for the highest-quality transport measurements. Probing FQH phases in scanning tunneling microscope (STM) measurements paves the way to explore these topological phases and their exotic excitations, including realization of methods for imaging anyons (*39*) or probing fractional edge states locally.

The spectroscopic measurements of the partially filled ZLL (Fig. 2A), including when the sample transitions through the FQH phases, always show splitting of the ZLL with a gap across the Fermi energy. This behavior is indicative of a Coulomb gap commonly observed when tunneling in and out of a two-dimensional electron gas at high magnetic fields (*40*–*42*). The strong correlations among electrons in the flat LLs dictate that additional energy is required for addition or removal of electrons from the system, resulting in a gap at the Fermi level that scales with the Coulomb energy $E_c = e^2/\varepsilon l_B$, where ε is the effective dielectric constant. The field dependence of this gap at partial filling follows the expected $\sqrt{B}$ behavior (Fig. 2C), tracing Coulomb energy E_c with a 0.62 scale factor, which agrees with the value obtained from our exact diagonalization calculations (*26*).

To directly visualize the broken valley symmetry of graphene's ZLL, we perform spectroscopic mapping of the electron and hole excitations of the ZLL (E-ZLL and H-ZLL, respectively) with V_B at the split ZLL peaks below or above the Coulomb gap. These spectroscopic *dI/dV* maps are performed with the STM tip at a constant height above the graphene, and hence they are directly proportional to the electron/hole excitation probability densities on the graphene atomic lattice. At filling ν = −2, the *dI/dV* map of electron excitations shows only graphene's honeycomb lattice, whereas at partial fillings between ν = −2 and −1, the *dI/dV* maps of hole excitations show sublattice polarization. A key feature of graphene's ZLL is that the electron states at the *K* or *K*′ valleys correspond to the A or B sublattice sites, respectively (*2*, *43*). Therefore, the sublattice polarization observed in these maps—for example, for hole excitation at ν = −1—is indicative of valley polarization in the ZLL, which agrees with the expectation of a spin- and valley-polarized ground state $|K'\uparrow\rangle$ at quarter-filling (*44*). The electron excitation at this filling shows partial polarization of the orthogonal state comprising $|K'\downarrow\rangle$, $|K\uparrow\rangle$, and $|K\downarrow\rangle$. Our measurements at fillings −2 < ν < −1 indicate that the ground state in this range also remains valley-polarized, thereby demonstrating that FQH states in this filling range are single-component and that valley symmetry breaking precedes the formation of FQH states (*45*).

Although valley polarization in the filling range −2 < ν ≤ −1 is dictated by interactions, we demonstrate that the sublattice asymmetry energy plays an important role in choosing which valley is occupied. In Fig. 2E, we extract the sublattice polarization $Z = (I_A - I_B)/(I_A + I_B)$, where I_A and I_B are the intensities of *dI/dV* signals at the A and B sublattices (*26*), and plot them for the ZLL as a function of filling.

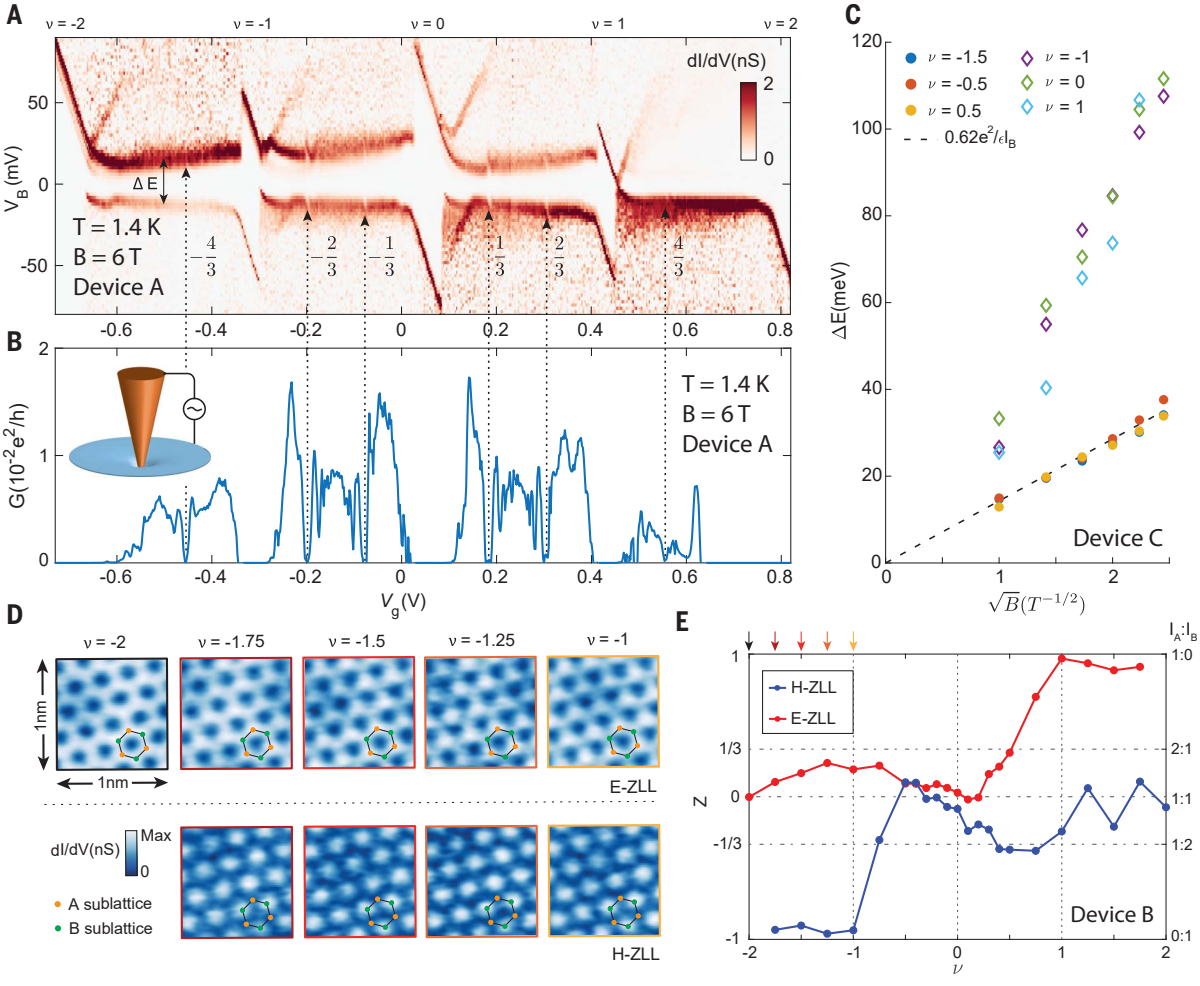

Fig. 2. Symmetry breaking and fractional quantum Hall states of the zeroth Landau level. (**A**) Tunneling spectrum of the zeroth Landau level between ν = −2 and 2 measured in device A. (**B**) Corbino transport measurement done on device A when contacting graphene with the tip by reducing tip height by 2 nm (B = 6 T, T = 1.4 K). Fractional states are detected from ν = 1/3 up to ν = 4/9. The gate voltages at which fractional features appear coincide with the tunneling measurement in (A). (**C**) The separations of the split ZLL peak as a function of $\sqrt{B}$, measured on device C. The splittings at half fillings scale with Coulomb energy (black dashed line). (**D**) *dI/dV* maps taken on the electron excitation of the ZLL (E-ZLL) and the hole excitation of the ZLL (H-ZLL) peaks at quarter-fillings between ν = −2 and −1 in device B. The hexagon pattern is the underlying graphene atomic lattice. The H-ZLL peak is fully sublattice-polarized in this filling range. (**E**) Sublattice polarization Z as a function of filling factors for H-ZLL and E-ZLL peaks extracted by Fourier transformation of *dI/dV* maps. Arrow colors correspond to those in (D).

Complementary to fillings in the range −2 < ν ≤ −1, where we find full polarization of the hole excitation, we find that for the range 1 ≤ ν < 2, the electron excitation maps probing the unoccupied states are fully polarized in the A sublattice. We find the occupied states, probed by the hole excitations, to be always polarized in the B sublattice regardless of the filling factor, as is evident from the blue line in Fig. 2E, which is almost entirely below zero. This behavior indicates that although interactions drive the symmetry breaking, the B sublattice is favored by an apparent AB sublattice asymmetry, likely originating from partial alignment with the hBN substrate.

We turn our attention to spectroscopic imaging at charge neutrality to show that electron interactions induce an intervalley coherent electronic state in half-filled ZLL at high fields. Spectroscopic maps of ν = 0 at 6 T (Fig. 3, A and B, device B) show a spatially varying electronic density with a periodicity that is $\sqrt{3}$ larger than that of the graphene lattice. This has been reported previously for graphene multilayers claimed to be decoupled, albeit without gate control (*46*). Such reconstruction of the unit cell, also referred to as the Kekulé distortion, is expected when an IVC phase forms. This state, which is one of the four anticipated phases at charge neutrality, has a real-space electronic wave function with probability density at both sublattices. To understand the real-space patterns for electron and hole excitations of this phase, we describe its valley order using a vector on a Bloch sphere: $|\psi\rangle = \cos(\theta/2)|K\rangle + \sin(\theta/2)\exp(i\phi)|K'\rangle$, with polar angle θ and azimuthal angle ϕ. For states with ordering vector pointing to the poles (θ = 0, 180°), electron densities correspond to full valley and sublattice polarization, forming a CDW state. In contrast, when the ordering vector lies along the equator of the Bloch sphere (θ = 90°), we have equal weight on both sublattices, with the azimuthal angle ϕ characterizing the phase coherence of the wave functions between the two sublattices. Computing the probability density $\langle\psi|\psi\rangle$, we find that the IVC state as described by ϕ = 0° and 180° (Fig. 3C) reproduces the Kekulé patterns seen experimentally for hole and electron excitation in Fig. 3, A and B, respectively. Naturally, the hole excitation has a real-space structure and valley polarization orthogonal to those of the electron excitation of the same state.

A more detailed analysis of the ordering vector as a function of the magnetic field reveals a continuous quantum phase transition

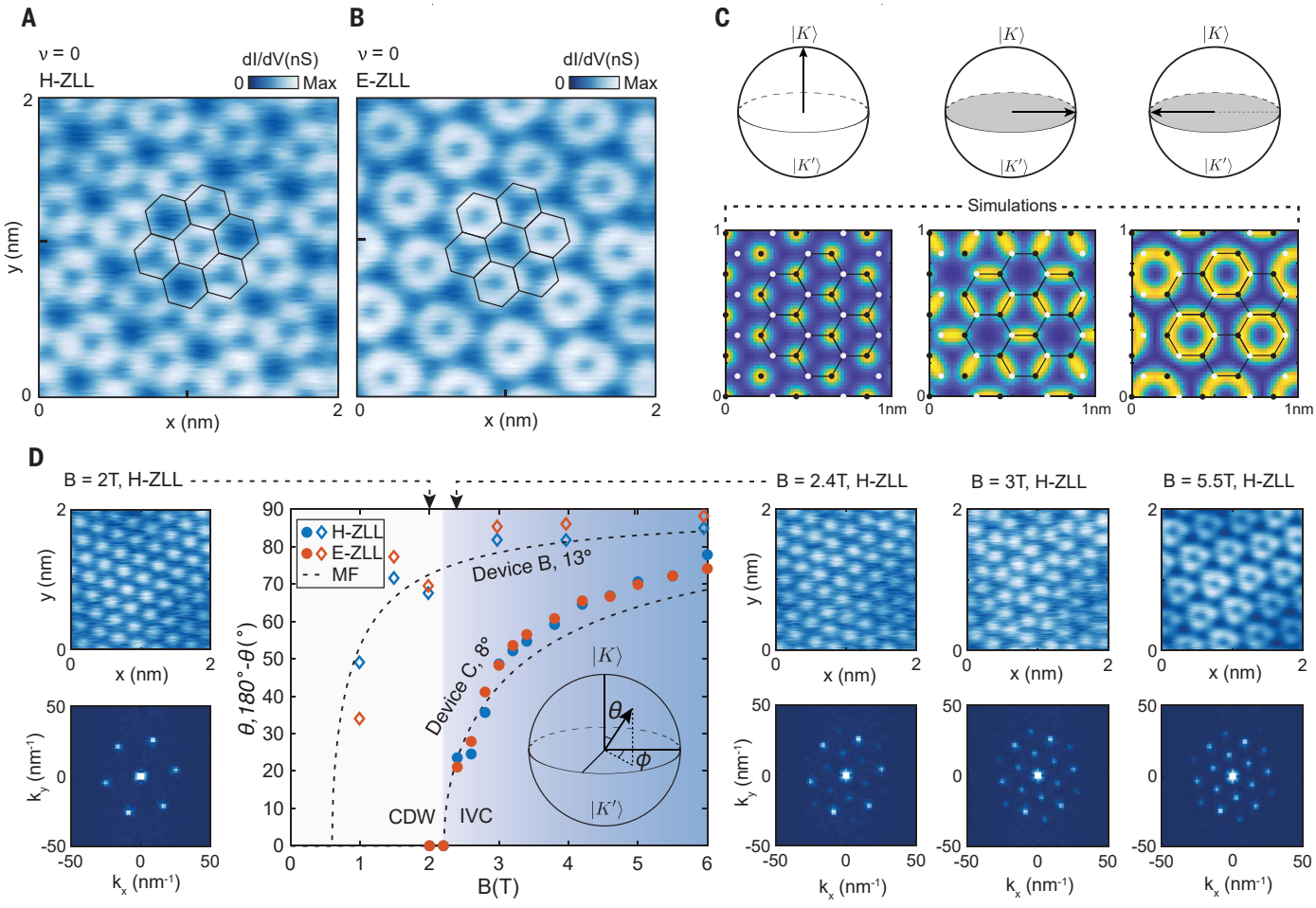

Fig. 3. Intervalley coherent state at the charge neutrality point. (**A** and **B**) *dI/dV* maps at the charge neutrality point, measured at B = 6 T in device B. The hexagons represent the graphene lattice. The *dI/dV* maps show a Kekulé reconstruction that triples the area of the unit cell. (**C**) Bloch sphere plot and corresponding simulated probability density of valley polarization for CDW (left) and IVC with ϕ of 0° (center) and 180° (right). (**D**) Main panel: Polar angle θ as a function of the magnetic field in devices B and C extracted from *dI/dV* maps. Plots are shown for θ (E-ZLL peaks) and 180° − θ (H-ZLL peaks). The complementary behavior of H-ZLL and E-ZLL peaks confirms their orthogonal nature. Device B has a 13° misalignment angle between the graphene and the hBN substrate; in device C this angle is 8°. The color shading of the background indicates the transition from CDW to IVC in device C. The mean field (MF) behavior for θ is shown as dashed lines, with critical fields of 2.2 T (device C) and 0.6 T (device B). Top side panels: *dI/dV* maps of the H-ZLL at a few representative magnetic fields in device C. Bottom side panels: Fourier transform of the *dI/dV* maps in the corresponding top panels. At B = 2 T, only Fourier peaks of the graphene lattice are visible, whereas at B = 2.4 T, Fourier peaks of the Kekulé pattern appear and increase in intensity with increasing magnetic field.

between the IVC Kekulé phase and the valley- and sublattice-polarized CDW state. We study this transition by extracting the ordering vector's polar angle θ from the Fourier transforms of real-space *dI/dV* maps and examine it as a function of the magnetic field. With increasing field, θ shows a continuous transition from the CDW phase (θ = 0) to an IVC state with θ approaching 90° in both devices (Fig. 3D). A critical field (2.2 T for device C) can be identified where θ becomes nonzero while intervalley coherence emerges, as detected by the appearance of Kekulé wave vectors in the FFT of *dI/dV* maps. We find that both the critical field and θ at 6 T measured in the two devices correlate with the influence of sublattice asymmetry imposed by the hBN substrate. The less aligned sample (device B, 13° misalignment between graphene and hBN lattice), with smaller sublattice asymmetry, shows a smaller critical field and approaches a pure IVC state with θ = 90° at a lower field than sample C. This behavior is consistent with the competition between the AB sublattice asymmetry, which favors one sublattice over the other, and valley anisotropy induced by short-range electron-electron and electron-phonon interactions (*18*), which favors valley polarization of θ = 90°. The magnetic field controls the strength of the interactions and in turn the valley anisotropy energy, thereby tuning θ like the order parameter of a continuous phase transition, a behavior well captured by a mean-field description (*26*) (Fig. 3D, dashed lines).

Finally, we show that measurements of the spatial variation of the ordering vectors in the IVC phase can be used to directly visualize the presence of topological excitations in this state. The spatial variations are extracted by performing local Fourier analysis on the *dI/dV* maps, where large areas of the sample show spatially independent θ and a constant gradient for ϕ. Uniform gradients in ϕ are expected in the presence of either strain or dilute short-range disorder (*25*). However, near charged defects on the graphene surface, likely caused by atomic adsorbates (Fig. 4A), we see markedly different behavior. Near this defect, we find that ϕ displays a swirl-like spatial variation (Fig. 4B), and the variation of θ plotted as sublattice polarization $Z = \cos(\theta)$ (Fig. 4C) displays a dipole-like feature. Analysis of higher-resolution electron excitation maps near this defect (Fig. 4D) shows the variations close to the defect of ϕ (with the linear gradient

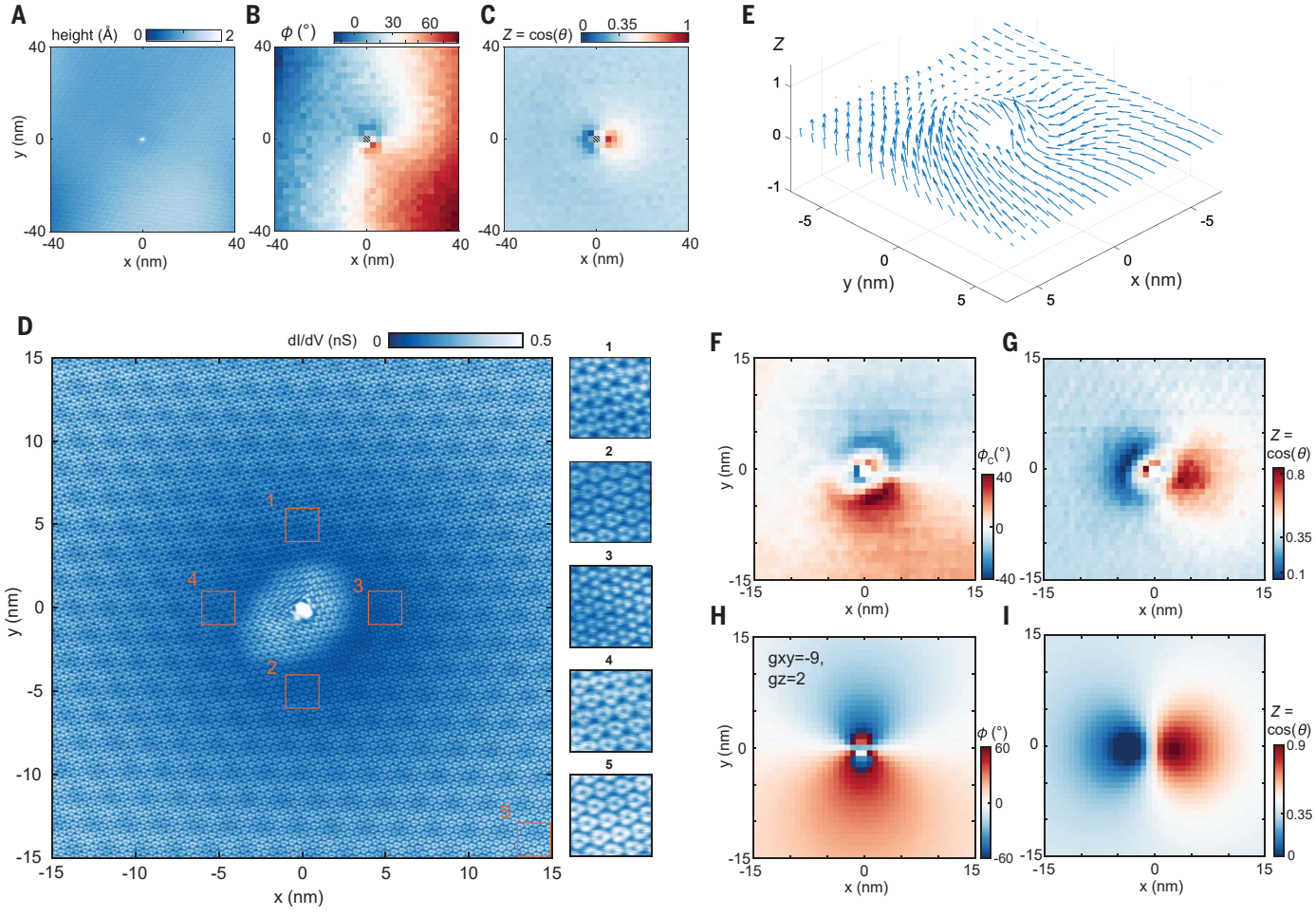

Fig. 4. Valley skyrmion of the IVC state near a charged defect. (**A**) Topography of the point defect found on device C. (**B** and **C**) Azimuthal angle ϕ and *Z* polarization extracted from *dI/dV* maps of the E-ZLL peak (*26*). (**D**) *dI/dV* map of the E-ZLL zoomed in the area near the defect shown in (A). Side panels: Magnified images of a few representative areas with matching labels. (**E**) Valley texture extracted from (D), visualized by arrays of arrows representing valley polarization in a Bloch sphere at each point. (**F** and **G**) Azimuthal ϕ and *Z* polarization extracted from (D). A linear background is subtracted from ϕ to produce ϕ_c (*26*). (**H** and **I**) Azimuthal angle and *Z* polarization extracted from a simulated map of electron density computed for a canted antiferromagnetic (CAF) skyrmion using the same Fourier procedure [see (*26*) for details of the calculations].

background subtracted) and *Z* more clearly (Fig. 4, F and G). A visual representation of the valley ordering vector texture near this defect is shown in Fig. 4E. This valley texture is consistent with that predicted for a CAF skyrmion excitation of the Kekulé phase (*23*). This topological excitation forms when the valley polarization of one spin species flips by 180° at its center, whereas the other spin species is devoid of any valley texture. The two key signatures of this skyrmion excitation are the dipole behavior in *Z*, which is equivalent to a meron-antimeron pair (Fig. 4I), accompanied by a dipole in ϕ oriented perpendicularly to the *Z* dipole (Fig. 4H). Simulating the valley texture using the nonlinear sigma model (NLSM) (*26*), we find excellent agreement between the results from the model calculations (Fig. 4, H and I) and our experimental results (Fig. 4, F and G). With our choice of model parameters, the calculation captures not only the qualitative behavior of φ and *Z* but also the size of the skyrmion, which is ~10 nm in both theory and experiment. This CAF skyrmion carries an electric charge of ±*e*, which is likely what caused their localization near a charged defect of the opposite sign. Our experiments show that besides the CAF skyrmion, other types of valley textures are also possible (fig. S5). Further work can map the zoo of predicted topological excitations in this and other QHFM phases of graphene (*22*, *23*). From a broader perspective, the microscopic approach to studying valley ordering can be applied to other two-dimensional systems, such as twisted bilayer graphene.

After submission, we have become aware of a related STM study of the ν = 0 state (*47*).

REFERENCES AND NOTES

1. Z. F. Ezawa, *Quantum Hall Effects: Field Theoretical Approach and Related Topics* (World Scientific, 2008).
2. B. I. Halperin, J. K. Jain, *Fractional Quantum Hall Effects: New Developments* (World Scientific, 2020).
3. K. P. Nuckolls *et al.*, *Nature* **588**, 610–615 (2020).
4. I. Das *et al.*, *Nat. Phys.* **17**, 710–714 (2021).
5. Y. Saito *et al.*, *Nat. Phys.* **17**, 478–481 (2021).
6. J. M. Park, Y. Cao, K. Watanabe, T. Taniguchi, P. Jarillo-Herrero, *Nature* **592**, 43–48 (2021).
7. Y. Choi *et al.*, *Nature* **589**, 536–541 (2021).
8. S. Wu, Z. Zhang, K. Watanabe, T. Taniguchi, E. Y. Andrei, *Nat. Mater.* **20**, 488–494 (2021).
9. B. E. Feldman *et al.*, *Science* **354**, 316–321 (2016).
10. M. T. Randeria *et al.*, *Nat. Phys.* **14**, 796–800 (2018).
11. S. L. Sondhi, A. Karlhede, S. A. Kivelson, E. H. Rezayi, *Phys. Rev. B* **47**, 16419–16426 (1993).
12. N. Nagaosa, Y. Tokura, *Nat. Nanotechnol.* **8**, 899–911 (2013).
13. H. Zhou, H. Polshyn, T. Taniguchi, K. Watanabe, A. F. Young, *Nat. Phys.* **16**, 154–158 (2020).
14. S. Chatterjee, N. Bultinck, M. P. Zaletel, *Phys. Rev. B* **101**, 165141 (2020).
15. S. Chatterjee, M. Ippoliti, M. P. Zaletel, arXiv 2010.01144 [cond-mat.str-el] (2020).
16. E. Khalaf, S. Chatterjee, N. Bultinck, M. P. Zaletel, A. Vishwanath, *Sci. Adv.* **7**, eabf5299 (2021).
17. J. G. Checkelsky, L. Li, N. P. Ong, *Phys. Rev. Lett.* **100**, 206801 (2008).
18. M. Kharitonov, *Phys. Rev. B* **85**, 155439 (2012).
19. A. Das, R. K. Kaul, G. Murthy, arXiv 2109.07515 [cond-mat.mes-hall] (2021).

20. A. F. Young *et al*., *Nature* **505**, 528–532 (2014).
21. H. Zhou *et al*., arXiv 2102.01061 [cond-mat.mes-hall] (2021).
22. Y. Lian, M. O. Goerbig, *Phys. Rev. B* **95**, 245428 (2017).
23. J. Atteia, Y. Lian, M. O. Goerbig, *Phys. Rev. B* **103**, 035403 (2021).
24. K. Nomura, S. Ryu, D. H. Lee, *Phys. Rev. Lett.* **103**, 216801 (2009).
25. C. Y. Hou, C. Chamon, C. Mudry, *Phys. Rev. B* **81**, 075427 (2010).
26. See supplementary materials.
27. J. Chae *et al*., *Phys. Rev. Lett.* **109**, 116802 (2012).
28. D. L. Miller *et al*., *Science* **324**, 924–927 (2009).
29. D. Walkup *et al*., *Phys. Rev. B* **101**, 035428 (2020).
30. S. Kim *et al*., *Nat. Commun.* **12**, 2852 (2021).
31. G. Li, A. Luican, E. Y. Andrei, *Phys. Rev. Lett.* **102**, 176804 (2009).
32. Y. J. Song *et al*., *Nature* **467**, 185–189 (2010).
33. D. L. Miller *et al*., *Nat. Phys.* **6**, 811–817 (2010).
34. S. Jung *et al*., *Nat. Phys.* **7**, 245–251 (2011).
35. A. Luican, G. Li, E. Y. Andrei, *Phys. Rev. B* **83**, 041405 (2011).
36. A. Luican-Mayer *et al*., *Phys. Rev. Lett.* **112**, 036804 (2014).
37. F. Ghahari *et al*., *Science* **356**, 845–849 (2017).
38. C. Gutiérrez *et al*., *Science* **361**, 789–794 (2018).
39. Z. Papić, R. S. K. Mong, A. Yazdani, M. P. Zaletel, *Phys. Rev. X* **8**, 011037 (2018).
40. J. P. Eisenstein, L. N. Pfeiffer, K. W. West, *Phys. Rev. Lett.* **69**, 3804–3807 (1992).
41. O. E. Dial, R. C. Ashoori, L. N. Pfeiffer, K. W. West, *Nature* **448**, 176–179 (2007).
42. O. E. Dial, R. C. Ashoori, L. N. Pfeiffer, K. W. West, *Nature* **464**, 566–570 (2010).
43. A. H. Castro Neto, F. Guinea, N. M. R. Peres, K. S. Novoselov, A. K. Geim, *Rev. Mod. Phys.* **81**, 109–162 (2009).
44. A. F. Young *et al*., *Nat. Phys.* **8**, 550–556 (2012).
45. C. R. Dean *et al*., *Nat. Phys.* **7**, 693–696 (2011).
46. S.-Y. Li, Y. Zhang, L.-J. Yin, L. He, *Phys. Rev. B* **100**, 085437 (2019).
47. A. Coissard *et al*., arXiv 2110.02811 [cond-mat.mes-hall] (2021).
48. X. Liu *et al*., Replication Data for "Visualizing Broken Symmetry and Topological Defects in a Quantum Hall Ferromagnet." Harvard Dataverse (2021); doi:10.7910/DVN/JZWE2C.

ACKNOWLEDGMENTS

We thank B. I. Halperin, A. H. Macdonald, N. P. Ong, and P. Kim for helpful discussions. **Funding:** Supported by NSF-DMR-1904442 and ONR-N00014-21-1-2592; Gordon and Betty Moore Foundation EPiQS initiative grant GBMF9469; NSF-MRSEC through the Princeton Center for Complex Materials NSF-DMR-2011750; DOE-BES grant DE-FG02-07ER46419; the Princeton Catalysis Initiative; the Elemental Strategy Initiative, Japan, grant JPMXP0112101001, JSPS KAKENHI grant JP20H00354, and CREST (JPMJCR15F3), JST (K.W. and T.T.); and the Army Research Office through the MURI program (grant W911NF-17-1-0323) (M.P.Z.). A.Y. acknowledges the hospitality of the Aspen Center for Physics, which is supported by NSF grant PHY-1607611, and Trinity College, where his stay was supported by a QuantEmX grant from ICAM and the Gordon and Betty Moore Foundation through grant GBMF9616. **Author contributions:** X.L., G.F., C.L.-C., and A.Y. designed the experiment. G.F., X.L., and C.L.-C. fabricated the sample. X.L., G.F., and C.L.-C. performed the measurements and analyzed the data. M.P.Z., Z.P., and X.L. conducted the theoretical analysis. K.W. and T.T. provided hBN crystals. X.L., G.F., C.L.-C., A.Y., and M.P.Z. wrote the manuscript with input from all authors. **Competing interests:** The authors declare no competing interests. **Data and materials availability:** The data from this study are available at the Harvard Dataverse (*48*).

SUPPLEMENTARY MATERIALS

science.org/doi/10.1126/science.abm3770
Materials and Methods
Supplementary Text
Figs. S1 to S7
References (*49*–*59*)

13 September 2021; accepted 17 November 2021
Published online 2 December 2021
10.1126/science.abm3770

Science

Visualizing broken symmetry and topological defects in a quantum Hall ferromagnet

Xiaomeng LiuGelareh FarahiCheng-Li ChiuZlatko PapicKenji WatanabeTakashi TaniguchiMichael P. ZaletelAli Yazdani

Science, 375 (6578), • DOI: 10.1126/science.abm3770

Looking for valley order in graphene

In addition to spin, electrons in the two-dimensional (2D) material graphene have the so-called valley degree of freedom. In the presence of strong magnetic fields, the state of the system can become spin or valley polarized, with several ground states proposed theoretically. This phenomenon has been explored through transport experiments. Liu *et al.* used scanning tunneling spectroscopy to take a closer look (see the Perspective by Morgenstern and Goerbig). Varying the magnetic field, the researchers observed signatures of two different ground states, as well as a skyrmion-like excited state. —JS